ELSEVIER

Cryogenics 39 (1999) 893–903

Cryogenics

"Electromaglev" ("active-maglev") – magnetic levitation of a superconducting disk with a DC field generated by electromagnets. Part 4: theoretical and experimental results on supercurrent distributions in field-cooled YBCO disks ☆

Makoto Tsuda *, Haigun Lee, So Noguchi [1], Yukikazu Iwasa

Francis Bitter Magnet Laboratory, Massachusetts Institute of Technology, Cambridge, MA 02139, USA

Received 12 April 1999; accepted 11 October 1999

Abstract

We present Part 4 results of a comprehensive theoretical study of an "electromaglev" system, in which a high-temperature superconducting bulk YBCO sample is levitated stably in a DC magnetic field generated by magnet system underneath the floating object. An electromagnetic analysis, based on a three-dimensional finite element technique (FEM) applied to the current vector potential method, has been developed to determine the supercurrent distribution in a field-cooled (and hence trapped-flux) YBCO disk that levitates stably in a magnetic field generated by the magnet system. The supercurrent distribution thus determined was in turn used to compute trapped-flux-induced field profiles of the disk and predict a "levitation current" in the magnet system at which the disk, initially resting on a support plate, begins to levitate. Agreement between computed field profiles and levitation currents and those measured in the experiment was excellent, validating the analysis itself and the method used to derive solutions. The analysis demonstrates that the supercurrent distribution within a trapped-flux disk is far more complicated than that derived from the Bean model for a long cylinder under a uniform axial magnetic field. It is used for a parametric study of the effects of disk dimensions (radius, thickness, radius/thickness ratio) and trapped-flux strength on supercurrent distribution and lift-to-weight ratio. The magnitude of the B_r component generated by the magnet system is very important for lift and it is shown that thinner disks rather than thicker disks can improve lift-to-weight ratio. Because accuracy of the analysis is disk-size independent, small disks are time-efficient for performing the analysis.

1. Introduction

We have been investigating an "electromaglev" ("active-maglev") system in which a superconducting bulk sample is levitated stably in a DC magnetic field generated by a magnet system [1–5]. Although levitation parameters such as levitation height and lift do not depend directly on the sample's superconducting critical current density, they do depend critically on the sample's size and geometry as well as on the applied magnetic field. Although field solutions for disk samples have been derived [6–8], they have not been applied in great detail to the active-maglev system. This paper presents analytical and experimental results of a study on supercurrent distribution and lift generated in YBCO disks, particularly on the dependence of supercurrent distribution and lift on disk parameters – radius, thickness, radius/thickness ratio, and strength of trapped flux.

The active-maglev system used to generate both experimental and analytical results consists of a YBCO disk and a magnet system comprised of an electromagnet and a set of steel plates. The electromagnet is comprised of two double pancake coils, each coil wound with silver-sheathed BSCCO-2223 tape; the steel plates on which the electromagnet rests enhance the field in the upper region of the space. The entire system is operated

☆ Work supported by the US Department of Energy, Office of Basic Sciences and in part by Daikin Industries MEC Laboratory, Tsukuba, Japan.

* Corresponding author.

[1] Visiting Scientist, May–July 1998. Department of Electrical Engineering, Waseda University, Tokyo, Japan.

0011-2275/00/$ - see front matter
PII: S0011-2275(99)00125-3

in a bath of liquid nitrogen. Two disk samples of the same diameter and different thicknesses were investigated in the experiment and analysis, and results, experimental and analytical, are compared. In the analysis presented in the previous paper [4], it is shown qualitatively that supercurrent in the disk flows at the disk's top and bottom layers as well as at the rim; the analytical results on lift derived from this supercurrent distribution agreed well with the experimental results. The previous analysis [4] is based on the assumption that the B_r component of the self field in the top layers and that in the bottom layers, both produced by the disk supercurrent, do not contribute much to lift because the "top lift" is nearly canceled by the "bottom lift". Similarly, the "top lift" and "bottom lift" due to the magnet system's field contribute a negligible amount to the main lift created at the rim. It is noted here that this good agreement achieved in the analysis is due in part to a specific range of dimensional parameters – radius, thickness, radius/thickness ratio – selected for those disks; it is not applicable for any arbitrary range of the parameters.

In a field-cool process, a disk, initially normal, becomes superconducting in the presence of an external magnetic field. When the external field is reduced to 0, the pinning centers in the disk trap the flux, leaving a trapped flux in the disk. Subsequently, when the external field is applied, a supercurrent flows over the disk's surface layers to shield the interior from this changing field.

Based on the Bean critical state model, as applied to a long cylinder exposed to a uniform external field, the penetration depth is determined only by the magnitude of external magnetic field at the rim, as is assumed in the zeroth-order theory [1–3]. That is, according to the zeroth-order theory the penetration depth for a given external field is the same for all disks regardless of their diameters. In a real active-maglev system such as the one used in this and earlier experiments, the disk is not a long cylinder nor is the external field generated by the magnet system uniform. The analytical study presented earlier [4] and continued here develops a numerical method to accurately compute this penetration depth, and hence lift and the levitation stability. Another important use of this analysis is in the study of active-maglev systems of multi-disk samples comprised of many small disks. We believe that such a multi-sample system will ultimately be used to generate "large" lift forces [5]. Ours adopts a three-dimensional finite element technique (FEM) based on the current vector potential (**T**) method [4,8,9]. Magnetic field profiles measured for each disk sample are compared with those computed by the analysis. Another key experimental parameter compared between experiment and analysis for a given set of operating conditions (disk dimensions, field-cool field) is the applied external field – expressed in terms of "levitation current" in the magnet system – at which the disk just begins to levitate. It is shown in the computed results that the disk supercurrent distribution is closely related not only to the magnitudes of both the external field and the trapped flux but to disk geometry. The analysis also shows that for a given external field at the rim, the penetration depth in each surface, top and bottom, depends on disk radius, thickness, radius/thickness ratio, and the disk material's critical current density (J_c). Specifically, for the same disk thickness, the penetration depth at the rim increases with radius; for the same disk radius, it decreases with thickness. The disk size effect is investigated in more detail through the study of "lift-to-weight ratios" for each "levitatee" that includes not only the lift-generating YBCO disk but also the load placed on it; in lift-to-weight ratio computation, only the weight of the lift-generating YBCO disk is included. The analytical results also indicate that for computing the supercurrent distribution in a disk it is the disk's radius/thickness ratio, not its radius or thickness, that is a key parameter. This has an important practical implication with "large" disks. Because the cost of FEM would be less and computation time shorter for a "small" disk than for a "large" disk, the numerical analysis of a large disk may be performed efficiently with a small disk having the same radius/thickness ratio as the large disk.

The effect of the magnitude of critical supercurrent density, J_c, on supercurrent distribution is also investigated. As is evident from the zeroth-order theory, the penetration depth generally decreases with critical supercurrent density, J_c. Also dependent on J_c are the disk's magnetic field profiles and the external magnetic field at which the disk starts to levitate; both increase with J_c but the rate of increase for each becomes smaller with J_c. These results in turn indicate that J_c in a superconducting disk sample can be deduced from measured field and lift data.

2. Experimental setup and procedures

Because supercurrent distribution cannot be measured directly, two sets of measurements were performed for each field-cooled disk: (1) field profile plots and (2) the "levitation current", I_{lev}, the current in the magnet system at which the disk begins to levitate. These experimental results are used to guide the analysis and verify the field profile plots and levitation current derived from the supercurrent distribution.

Fig. 1 is a schematic drawing of the cross-sectional view of an active-maglev system used in the experiment. In the figure, a YBCO disk, $2R_d$ in diameter and δ_d thick, is shown afloat on the axis of and above a magnet system, which is an electromagnet, comprised of a two double pancake coils each wound with silver-sheathed

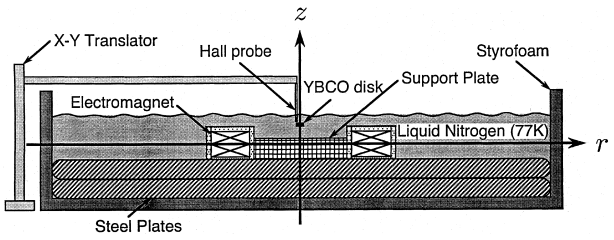

Fig. 1. A schematic drawing of the cross-sectional view of an active-maglev system used in the experiment.

BSCCO-2223 tape, placed on steel plates. Placed in the bore of the electromagnet is a support plate on which the YBCO disk rests when it is not afloat. The entire system is placed in a Styrofoam container filled with liquid nitrogen boiling at 77 K. The key parameters of the magnet system are given in Table 1. Also shown in the figure is a Hall probe placed in the liquid just above the disk and attached to an X–Y translator located outside the Styrofoam container.

The experiment proceeds through the following steps:

1. Place a YBCO disk, initially in the normal state, on the support plate in the presence of an external field generated by "field-cool" current, I_{fc}, in the magnet system.
2. With the disk in the superconducting state, reduce the magnet current to 0. The disk is now in zero external field but with a trapped flux, producing a magnetic field.
3. Map this field at specific distances above the disk's upper surface with the Hall probe. Each set of field plots gives the axial component of the field, B_z, at a fixed axial location, z_j, as a function of radial position, r, i.e., $B_z(z_j, r)$.
4. Increase the magnet current, initially at 0, to "levitation" current, I_{lev}, at which the disk, resting on the support platform, begins to levitate.

In this experiment each field-cooled ($I_{fc} = 10$ A) YBCO disk was examined for its field symmetry about the z-axis, because only those disks with this symmetry could be used to test the analysis. Indeed there were a few disks that showed an unmistakable asymmetry in the field profiles, implying the presence of defects within these disks. Among those disks having field symmetry, two disks were selected for the experiment, one with $R_d = 5$ mm and $\delta_d = 2$ mm – designated $Disk_{5/2}$ – and the other $R_d = 5$ mm and $\delta_d = 4$ mm, $Disk_{5/4}$. For both disks, the magnetic field profiles were measured at magnet currents of 0 and 10 A after field-cooled at $I_{fc} = 10$ A, while I_{lev} was measured for I_{fc} of 7, 10, and 13 A.

Table 1
Magnet system parameters

Parameter	Value
Winding (coil form) i.d. (mm)	70 (66)
Winding (coil form) o.d. (mm)	123 (127)
Winding (coil form) height (mm)	17 (22)
Number of double pancake	2
Total number of turns	364
Nominal maximum I_{op} (A)	19
Field at $(0,0)$ @19 A	0.157
Steel plate o.d. (thickness) (mm)	340 (25)

3. Formulation

3.1. FEM

As mentioned above, to derive the conditions of lift and stability more rigorously, the supercurrent distribution in a field-cooled YBCO disk must be determined more accurately. In the previous paper [4], we developed a method to determine the supercurrent distribution and I_{lev} values both of which agreed well with experimental values. When comparison was extended to include field profile data, however, the earlier method proved inadequate. We believe this inadequacy stems from inaccuracy in the supercurrent distribution. Specifically, we believe that a conventional method based on the Bean critical state model applied to an infinitely long cylinder does not lead to a valid supercurrent distribution in a disk. Therefore, a three-dimensional FEM based on the current vector potential (**T**) method [4,8,9] has been adopted in this study, with the effect of disk geometry included. The current vector potential **T** is defined by

$$\nabla \times \mathbf{T} = \mathbf{J}, \tag{1}$$

$$\nabla \cdot \mathbf{T} = 0 \quad \text{(Coulomb gauge)}, \tag{2}$$

$$\mathbf{n} \times \mathbf{T} = 0 \quad \text{(on the surface)}. \tag{3}$$

Using the Helmholtz formula, we derive the governing equation

$$\nabla \times \frac{1}{\sigma_s} \nabla \times \mathbf{T} + \mu_o C_p \frac{\partial \mathbf{T}}{\partial t} + \frac{\mu_0}{4\pi} \int_S \frac{\partial T_n}{\partial t} \nabla \left(\frac{1}{r} \right) \mathrm{d}S = -\frac{\partial \mathbf{B}_0}{\partial t}, \tag{4}$$

where **n** is the directional vector normal to the surface; σ_s is, as discussed below, an "appropriate" conductivity of the superconductor; C_p the ratio of solid angle to 4π; T_n the current vector potential in the n-direction; r is the distance between source and point of computation; and $\mathbf{B}_0$ is the magnetic flux density generated by the magnet system. The magnetic flux density, $\mathbf{B}_0$, is calculated by an equivalent current method (ECM) [4,10].

Based on the assumption that both the disk sample and the magnetic field distribution produced by the

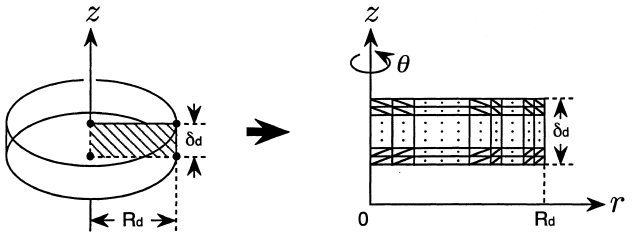

Fig. 2. Left-hand side: rectangular cross-section of the disk, sliced axially in the radial direction from the center to R_d; right-hand side: rectangular plane is segmented into right-angled triangle elements.

magnet system are symmetric with respect to the z-axis, Eq. 4 can be solved as a axisymmetric problem, as shown in Fig. 2. Here a rectangular cross-section of the disk, sliced axially in the radial direction from the center to R_d (left-hand side of Fig. 2), is segmented into right-angled triangular elements (right-hand side of Fig. 2). To take into account that supercurrent is concentrated at the rim, smaller elements are used near the rim. Supercurrent density is evaluated at each element's center of gravity and assigned for the entire element. In applying this conventional eddy current approach to shielding supercurrent analysis, we use the following constituent equations [9]:

$$\mathbf{J} = \sigma_s \mathbf{E}, \quad \sigma_s = \frac{J_c}{|\mathbf{E}|} \qquad (\mathbf{E} \neq 0), \tag{5}$$

$$\frac{\partial \mathbf{J}}{\partial t} = 0 \quad (\mathbf{E} = 0). \tag{6}$$

The numerical scheme follows an iterative process in which the conductivity of each element is adjusted to make the amplitude of the current density in that element equal to J_c. Note that J_c is assumed constant throughout the disk. As explained in the previous paper [4], penetration depths at the top and bottom surfaces are relatively small compared with that at the rim. Therefore, the number of elements in the z-axis direction is also very important to properly model the thin penetration depth at each surface.

Considering this requirement of penetration depth at each surface and a computer memory restriction, we arrived at an adequate number of meshes to insure a certain degree of accuracy in our solutions through repeated calculations, each time with a different mesh size. Based on the solution of $\mathbf{T}$ in Eq. 4, supercurrent density in each element is calculated through Eq. (1). The total magnetic flux density inside the disk, $\mathbf{B}_{all}$, is given by

$$\mathbf{B}_{all} = \mathbf{B}_0 + \mathbf{B}_e = \mathbf{B}_0 + \mu_0 C_p \mathbf{T} + \frac{\mu_0}{4\pi} \int_S T_n \nabla \left(\frac{1}{r} \right) dS, \tag{7}$$

where $\mathbf{B}_0$ is the magnetic flux due to the magnet system and $\mathbf{B}_e$ is the magnetic flux density induced by the disk's supercurrent. Using the $\mathbf{B}_{all}$, we obtain an expression for lift, F_z:

$$F_z = \int_V -J_\theta B_{r_{all}} \, dV = \sum_{e=1}^{Ne} -2\pi J_\theta(e) \int_e B_{r_{all}} r \, dr \, dz, \tag{8}$$

where Ne is the number of elements and $B_{r_{all}}$ is the r-component of the total magnetic flux density produced by the magnet system and the disk's supercurrent.

4. Results and discussion

4.1. Magnetic field Profiles

Fig. 3 presents $B_z(r, \Delta z)$ plots for field-cooled ($I_{fc} = 10$ A) $Disk_{5/2}$ resting on the support plate; the symbols are measured data and lines are computed. In each set symbols are measured and lines are computed; error bars indicate uncertainties in the measured field data. The three lower sets of plots are with the magnet at 0 A,

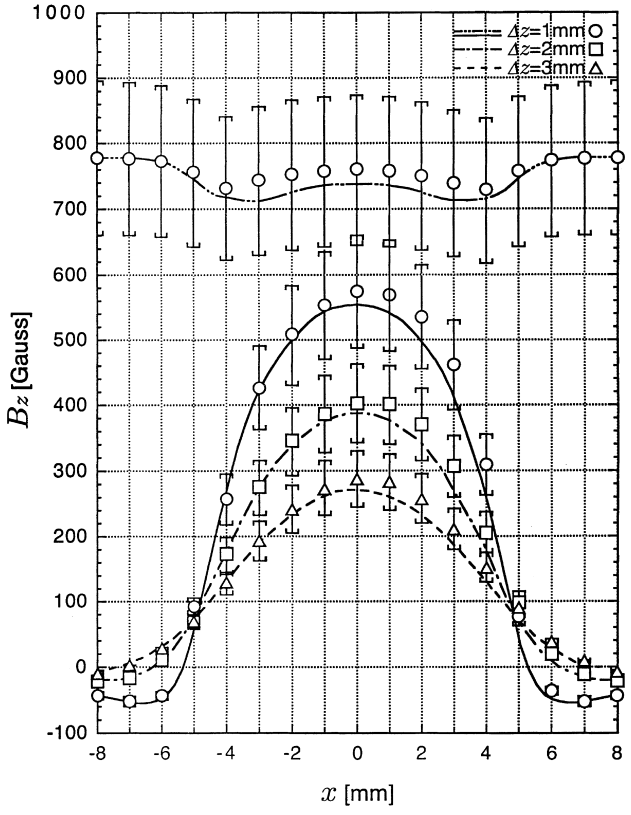

Fig. 3. $B_z(r, \Delta z)$ plots for field-cooled ($I_{fc} = 10$ A) $Disk_{5/2}$ resting on the support plate. In each set symbols are measured and lines are computed; error bars indicate uncertainties in the measured field data. The three lower sets of plots are with the magnet at 0, while the top set is with the magnet charged to 10 A. Data points and corresponding lines at the following values of Δz: circles, 1 mm; squares, 2 mm; triangles, 3 mm.

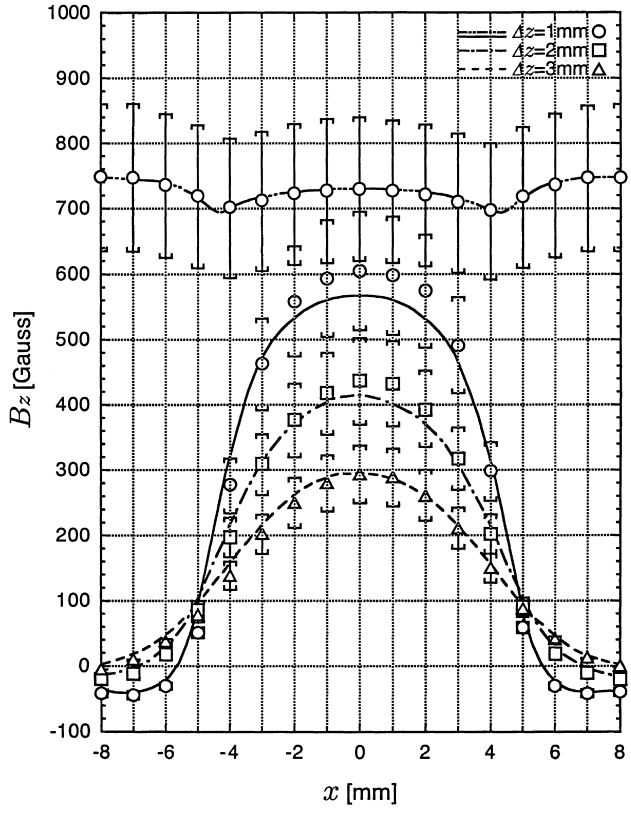

Fig. 4. $B_z(r,\Delta z)$ plots for field-cooled ($I_{fc} = 10$ A) $Disk_{5/4}$ resting on the support plate. Note that because $D_{5/4}$ is 2 mm thicker than $D_{5/2}$, the Hall probe location in Fig. 4 is higher than 2 mm for the same values of Δz in Fig. 3.

while the top set is with the magnet charged to 10 A. Data points and corresponding lines at the following values of Δz: circles, 1 mm; squares, 2 mm; triangles, 3 mm Fig. 4 presents similar plots for $Disk_{5/4}$ with the symbols and curves corresponding to those in Fig. 3. Note that because $Disk_{5/4}$ is 2 mm thicker than $Disk_{5/2}$, the Hall probe location in Fig. 4 is higher than 2 mm from the center $(0,0)$ for the same values of Δz in Fig. 3.

In both Figs. 3 and 4 error bars indicate uncertainties in the measured field data. Agreement between measurement and computation is quite good, confirming that the supercurrent distribution used in the analysis is valid.

4.2. Lift

For each disk an average value of I_{lev} was determined from several measurements for each of field-cool currents I_{fc} of 7, 10, and 13 A. The average values of I_{lev} for both disks are given in Table 2. In the analysis, I_{lev} is defined as the magnet current at which lift, F_z, is equal to the disk weight, $M_d g$, modified to include the buoyancy of liquid nitrogen

$$F_z = (M_d - V_d \varrho_{LN_2}) g, \tag{9}$$

Table 2
Measured and computed values of I_{lev} for $Disk_{5/2}$ and $Disk_{5/4}$

δ_d (mm)	I_{lev} (A)		
	$I_{fc} = 7$ A	$I_{fc} = 10$ A	$I_{fc} = 13$ A
2	9.4	11.7	13.9
	(9.5)[a]	(11.8)	(13.8)
4	10.4	12.6	14.9
	(10.6)	(12.5)	(14.7)

[a] Values in parentheses are computed.

where M_d and V_d are, respectively, the disk's mass and volume and ϱ_{LN_2} is the density of liquid nitrogen. The analytical values of I_{lev} for both disks are also presented in Table 2. Here too agreement between measurement and computation is quite good. This good agreement, along with the good agreement achieved in field profile, strongly validates the method used in the analysis to determine supercurrent distribution.

4.3. J_c: a parametric study

In the analytical results presented above, a value of 3×10^8 A/m^2 was chosen for J_c because the supercurrent distributions that resulted from it gave field profiles and I_{lev} values that agreed well with experimental results. We present here results of a parametric study of J_c on field profiles and I_{lev}. Such a study is important because in a real active-maglev system that is to generate a large lift force, a disk configuration of either a single YBCO disk with a diameter exceeding ~300 mm or multiple disks each no greater than 100 mm would be required [5]. The latter configuration is more likely, and to make the matter even more complicated, there will unquestionably be a variation in J_c among these disks, which may negatively impact the levitation performance.

Fig. 5 shows $\Delta B_z(r;J_c,J_{c_0})$ plots for field-cooled ($I_{fc} = 10$ A) $Disk_{5/2}$ at J_c values of 1×10^8, 2×10^8, 4×10^8, and 5×10^8 A/m^2, with a reference J_{c_0} at 3×10^8 A/m^2. Here $\Delta B_z(r;J_c,J_{c_0})$ is defined as the difference in $B_z(r)$ corresponding to J_c and that corresponding to J_{c_o}. The plots in Fig. 5(a) are with the magnet idle, while those in Fig. 5(b) are with the magnet charged to 10 A. Both Fig. 5(a) and (b) show that values of $|\Delta B_z|$ are significantly greater when $J_c < J_{c_0}$ than when $J_c > J_{c_0}$. We believe that this asymmetry of $|\Delta B_z(r)|$ with $J_{c_0} - J_c$ sign is attributable to the size of the penetration depth – the greater the J_c the thinner the penetration depth generally will be and the field profile approaches rapidly the asymptote profile of an infinitely thin penetration depth. This influence of penetration depth thickness can also be observed as the ΔB_z maximum, which occurs near $r = 4$ mm in each plot, moves towards the rim with

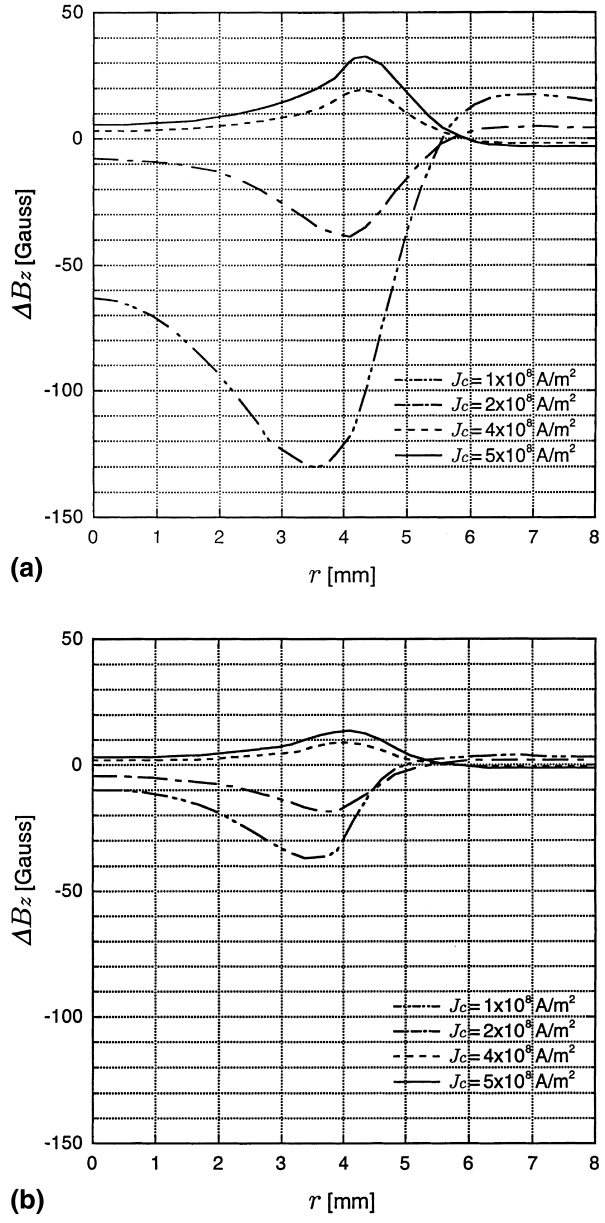

Fig. 5. $\Delta B_z(r;J_c,J_{c_0})$ plots for field-cooled (I_{fc} = 10 A) $Disk_{5/2}$ for J_c values of 1×10^8, 2×10^8, 4×10^8 and 5×10^8 A/m^2, with a reference J_{c_0} at 3×10^8 A/m^2. $\Delta B_z(r;J_c,J_{c_0})$ is defined as the difference in $B_z(r)$ corresponding to J_c and that corresponding to J_{c_0}. (a) Magnet system idle; (b) magnet system charged at 10 A.

increasing J_c and also as the ΔB_z minimum, which too occurs near $r = 4$ mm moves towards the center with decreasing J_c. The maximum/minimum locations of $r \sim 4$ mm for $Disk_{5/2}$ imply that for a 10 mm $\varnothing$ disk the most effective locations for field measurement, if the measurement is to be limited only to a few spots, are in the vicinity of $r \sim 4$ mm. Because the external field of the magnet obviously obscures the disk's own field, the dependence of ΔB_z on J_c is more evident with the magnet idle (Fig. 5(a)) than with the magnet energized (Fig. 5(b)).

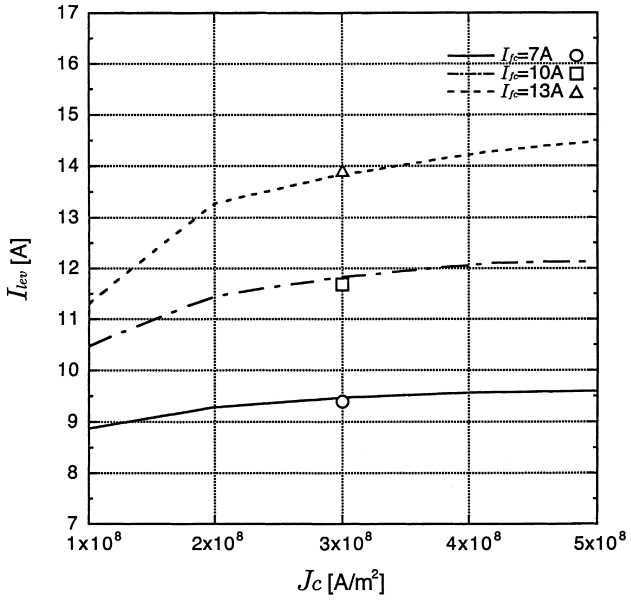

Fig. 6. I_{lev} vs J_c plots for $Disk_{5/2}$ at three different field-cool currents, I_{fc} of 7, 10, and 13 A; points are experimental.

Fig. 6 shows I_{lev} vs J_c plots for $Disk_{5/2}$ at three different field-cool currents, I_{fc} of 7, 10, and 13 A; three points are experimental. Again, as the penetration depth converges towards zero thickness with increasing J_c, I_{lev} approaches an asymptote for each I_{fc}. Values of J_c determined from experimental values of I_{lev} are 2.6×10^8, 2.6×10^8, and 3.2×10^8 A/m^2 for I_{fc}, respectively, of 7, 10, and 13 A; all are off slightly from J_{c_0}.

4.4. Supercurrent distribution in field-cooled disk

Fig. 7 shows supercurrent density distributions, in the rectangular z–r plane, for field-cooled ($I_{fc} = 10$ A)

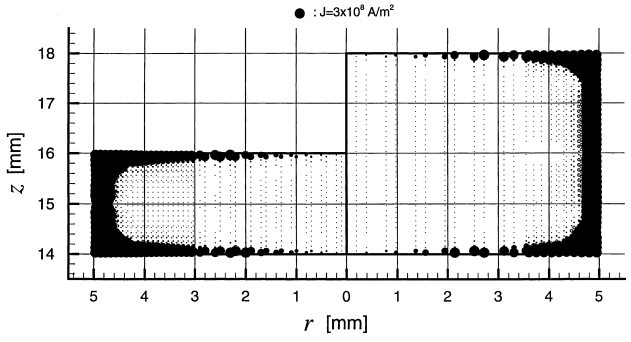

Fig. 7. Supercurrent density distributions, in the rectangular z–r plane, for field-cooled (I_{fc} = 10 A) $Disk_{5/2}$ (left) and $Disk_{5/4}$ (right) with the magnet idle.

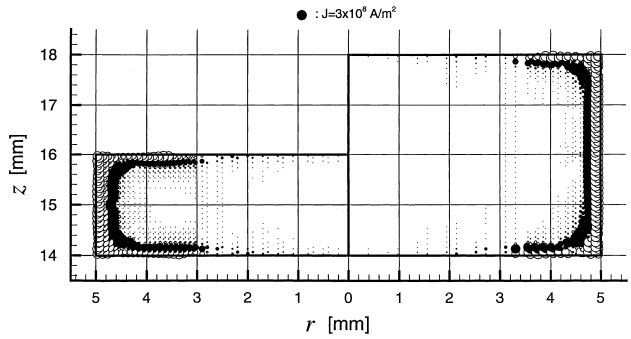

Fig. 8. Supercurrent density distributions of $Disk_{5/2}$ (left) and $Disk_{5/4}$ (right) for $I_{fc} = 10$ A and the magnet recharged to 10 A.

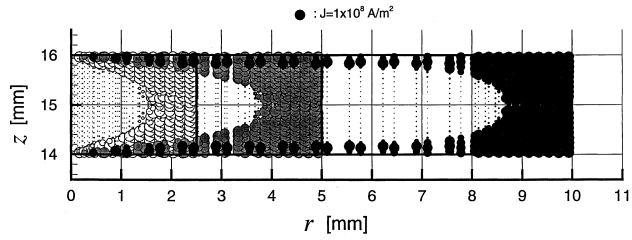

Fig. 9. Supercurrent distributions for 2 mm thick disks of three radii: $Disk_{2.5/2}$ (white circles for J); $Disk_{5/2}$ (gray for J); and $Disk_{10/2}$ (black for J).

$Disk_{5/2}$ (left) and $Disk_{5/4}$ (right) with the magnet idle. Fig. 8 shows similar results ... recharged to 10 A. In these and subsequent ... highlighted bullet (3×10^8 A/m^2). For example, $Disk_{5/2}$ with $I_{fc} = 10$ A and zero magnet current (Fig. 7 left-hand side distribution), small bullets near the top and bottom surfaces in the region $r < 2$ mm indicate that J in this region is much smaller than 3×10^8 A/m^2; tiny dots over the entire interior area furthermore signify, unlike the Bean critical state model, the ubiquitous presence of very small but nonetheless non-zero supercurrent over the entire body of the disk.

Note that the penetration regions in the top and bottom surfaces increase their depth with r, converging with the penetration region at the rim, which is relatively constant in the z-axis. This constant penetration depth with z at the rim is more evident with a thicker disk, $Disk_{5/4}$ (Fig. 7 right-hand side distribution). Although both disks are exposed to ... greater than $Disk_{5/4}$'s. $Disk_{5/2}$'s penetration depth is greater because ... top and bottom surfaces. As evident from Fig. 8, thinner disk ($Disk_{5/2}$, left-hand side distribution) and thicker disk ($Disk_{5/4}$, right-hand side distribution), and also predictable from the Bean model, an induced supercurrent flows in the opposite direction when the magnet is re-energized, in this case from 0 to 10 A.

4.5. Disk parameters on supercurrent distribution

Unlike an infinitely long cylinder under a uniform axial magnetic field, a disk, as seen in Figs. 7 and 8 for $Disk_{5/2}$ and $Disk_{5/4}$, has a supercurrent distribution that is quite complicated. It depends not only on external magnetic field but also the disk's geometry and the strength of its trapped flux. Although results of $Disk_{5/2}$ and $Disk_{5/4}$ have already depicted supercurrent distributions for disk-shaped samples in general, the effects of a disk's specific parameters have not been addressed. These parameters include radius, thickness, radius/thickness ratio, and strength of trapped flux are discussed below.

In the results presented below in which dependence of supercurrent distribution on each of these disk parameters is analyzed, we have set $J_c = 1 \times 10^8$ A/m^2, rather than $J_{c_0} = 3 \times 10^8$ A/m^2, to amplify the effect of each parameter on supercurrent distribution. Also kept constant in the analysis is the external field, which is also assumed uniform.

Radius: Fig. 9 shows supercurrent distributions for 2-mm thick disks of three radii: $Disk_{2.5/2}$ (white circles for J); $Disk_{5/2}$ (gray for J); and $Disk_{10/2}$ (black for J). Even with the external field being held constant, thickness of the penetration depth at the rim increases with disk radius. This is because the greater the disk size, the larger becomes the interior area, hence more supercurrent is required, which in turn requires a larger penetration depth.

Thickness: Fig. 10 shows supercurrent distributions for 5-mm radius disks of three thicknesses: $Disk_{5/1}$ (white circles for J); $Disk_{5/2}$ (gray); and $Disk_{5/4}$ (black). Here the penetration depths at the top and bottom surfaces decrease with thickness; the same trend is observed for the penetration depth at the rim. That is, the thicker the disk, the closer it approaches the "Bean disk," which is an infinitely long cylinder.

Trapped field: The penetration depth also changes with I_{fc} and magnet current. Fig. 11 presents supercurrent distributions in $Disk_{5/2}$ for field-cool currents of: 5 A (white circles for J); 10 A (gray); and 20 A, (black), all at zero magnet current. The penetration depths at all three surfaces become thicker with trapped flux, virtually making at $I_{fc} = 20$ A the region of constant penetration depth at the rim disappear. These results appear to imply that the smaller the trapped flux, the finer mesh sizes are required to accurately map the supercurrent distribution. Also, it is noted that the smaller the trapped flux, the better the distribution resembles the Bean distribution.

Radius/thickness ratio: By displaying supercurrent distributions of several disks of different radius,

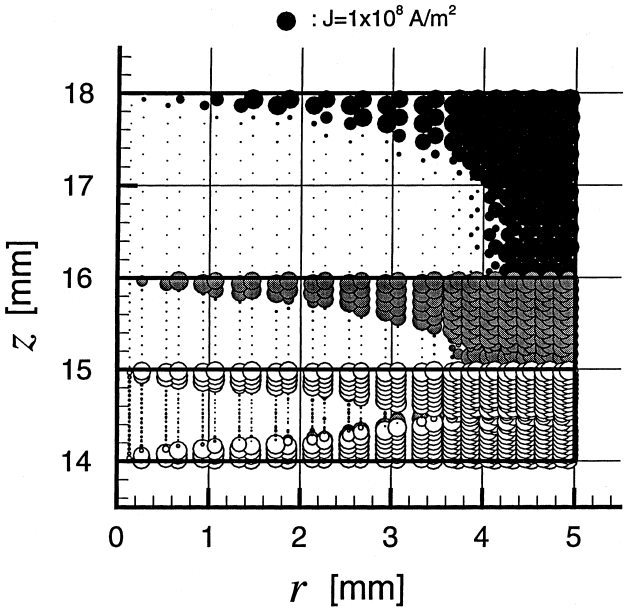

Fig. 10. Supercurrent distributions for 5 mm radius disks of three thicknesses: $Disk_{5/1}$ (white circles for J); $Disk_{5/2}$ (gray); and $Disk_{5/4}$ (black). Note that both black and gray circles are clearly visible only over the upper half of respective disks.

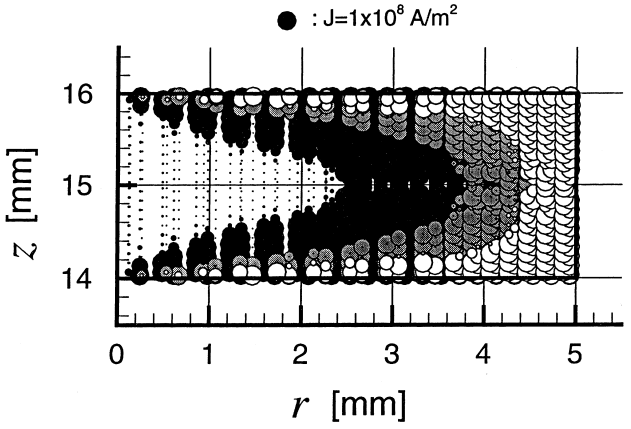

Fig. 11. Supercurrent distributions in $Disk_{5/2}$ for three field-cool currents of: 5 A (white circles for J); 10 A (gray); and 20 A (black), all at zero magnet current. Note that both black and gray circles are masked over most of the region.

thickness, and trapped flux, we have demonstrated the dependences of supercurrent distribution on these disk parameters. To further this parametric study, we present here results for disk radius/thickness ratios of 2.5 and 1.25 with the following disks: $Disk_{2.5/1}$ (2.5 mm radius, 1 mm thickness), $Disk_{5/2}$, $Disk_{10/4}$; $Disk_{1.25/1}$, $Disk_{2.5/2}$, $Disk_{5/4}$.

The magnetic flux density within a disk, $\mathbf{B}_{e_0}$, due to its supercurrent is obtained by the Biot–Savart law

$$\mathbf{B}_{e_0} = \frac{\mu_0}{4\pi}\int_V \frac{\mathbf{J}\times\mathbf{R}_{QP}}{R_{QP}^3}\mathrm{d}V, \tag{10}$$

where $\mathbf{R}_{QP}$ is the vector directed from source point to field point with $|R_{QP}|$ representing the distance between them and $\mathbf{J}$ is supercurrent density, which is assumed constant. In Eq. 10, we further assume that the relative position of the supercurrent flowing region and non-flowing region is the same in each disk. When both radius and thickness are increased by a factor of n, then so are $\mathrm{d}V$, and R_{QP}, resulting in $\mathbf{B}_{e_0}$, which is n times the original. This implies that if radius, thickness, trapped field, and $\mathbf{B}_{e_0}$ are each increased by n, the size of each right-angled triangular element, current-carrying or not, is increased by n as well as the element's z and r distances from the reference point. That is, the supercurrent's total area (in the disk's cross-section) is increased by n^2 and its distribution relative to reference points, e.g., the four corners of the rectangular plane, remain the same: penetration depth at every surface becomes n times thicker than the original.

Fig. 12 shows a supercurrent distribution for $Disk_{2.5/1}$, which has a radius/thickness ratio of 2.5, with $J_c = 1\times10^8$ A/m^2. Similarly, Fig. 13 shows a distribution for $Disk_{1.25/1}$, which has a radius/thickness ratio of 1.25, with $J_c = 1\times10^8$ A/m^2. In Fig. 12, distributions for $Disk_{5/2}$ and $Disk_{10/4}$, also of a radius/thickness ratio of 2.5, have been omitted because they look similar to that of $Disk_{2.5/1}$. For the same reason distributions for $Disk_{2.5/2}$ and $Disk_{5/4}$, both having the same radius/thickness ratio as $Disk_{1.25/1}$ have been omitted in Fig. 13. The results of Figs. 12 and 13 demonstrate that supercurrent distribution is invariant with both radius and thickness if their ratio remains a constant. The results further indicate that supercurrent distribution can be obtained with the same degree of accuracy regardless of

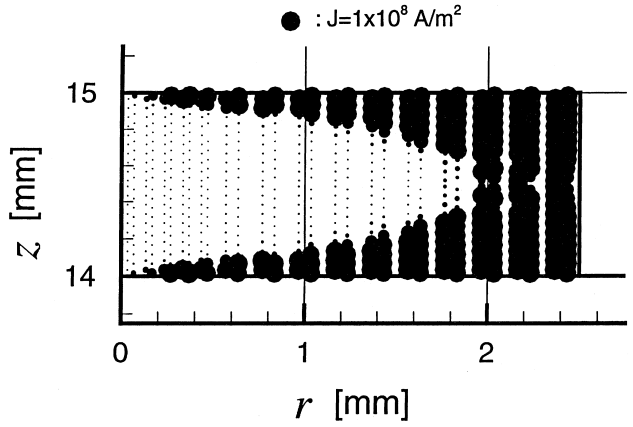

Fig. 12. Supercurrent distribution for $Disk_{2.5/1}$ (radius/thickness: 2.5) with $J_c = 1\times10^8$ A/m^2.

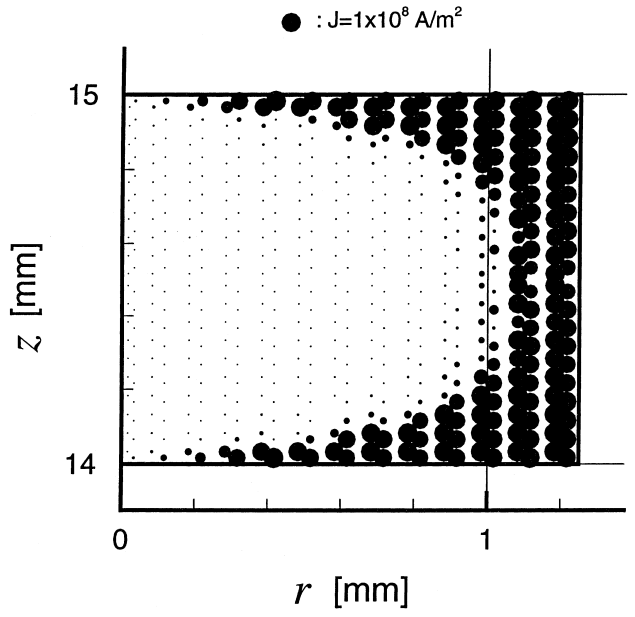

Fig. 13. Supercurrent distribution for $Disk_{1.25/1}$, (radius/thickness: 1.25) with $J_c = 1 \times 10^8$ A/m^2.

disk radius; what matters is the radius/thickness ratio. Because in a typical FEM analysis, the number of elements required is proportional to disk size, the analysis becomes more time-efficient with small disks.

4.6. Lift-to-weight ratio

Lift-to-weight ratio, $f_{l/w}$, is an important performance parameter of the active-maglev system; it is defined as the ratio of a lift force F_z created in the YBCO disk to the disk weight, $M_d g$:

$$f_{l/w} \equiv \frac{F_z}{M_d g}. \tag{11}$$

In a practical active-maglev system its electromagnet current must exceed I_{fc} to generate F_z that is greater than $M_d g$, because the disk must generally carry a load. There are two sources of the r-component of the magnetic induction that interacts with the disk supercurrent and generates F_z: (1) $B_{r_{mag}}$, generated by the magnet system and (2) $B_{r_{dsk}}$, generated by the disk supercurrent. The lift due to $B_{r_{mag}}$, $F_{z_{mag}}$, is given by

$$F_{z_{mag}} = \int_V -J_\theta B_{r_{mag}} \, dV = \sum_{e=1}^{Ne} -2\pi J_\theta(e) \int_e B_{r_{mag}} r \, dr \, dz. \tag{12}$$

For electromagnet currents that exceed I_{fc}, the system achieves $F_{z_{mag}} > M_d g$ or $f_{l/w} > 1$. (The lift due to $B_{r_{dsk}}$ is too small to lift the disk itself.) We may define $f_{m/l}$ as the ratio of $F_{z_{mag}}$ to F_z:

$$f_{m/l} \equiv \frac{F_{z_{mag}}}{F_z}. \tag{13}$$

The larger the $f_{m/l}$, the less will be the dependence of lift on supercurrent.

Fig. 14 presents $f_{l/w}$ and $f_{m/l}$ for seven disks ($I_{fc} = 10$ A), each with a magnet current of 10 A ($= I_{fc}$), i.e., $f_{l/w} < 1$. Although $f_{l/w}$ for a given thickness is relatively constant with radius, for a given radius it decreases with thickness. Dependences of $f_{rmm/l}$ on dimensions, on the other hand, are just the reverse: for a given thickness it increases with radius and for a given radius, it is nearly constant with thickness.

The relationship between radius and $f_{l/w}$ is more complicated than between thickness and $f_{l/w}$. This is because the change of $B_{r_{all}}$ in the r-direction, which is much larger than that in the z-direction, affects the magnitude of lift greatly. $f_{l/w}$ depends on relative increasing rates between weight and magnitude of $B_{r_{all}}$ in the region where supercurrent is flowing. Referring to Fig. 14, note that comparing $Disk_{5/2}$ with $Disk_{2.5/2}$, both 2 mm thick disks, $Disk_{5/2}$ has a smaller $f_{l/w}$ than $Disk_{2.5/2}$. On the other hand, comparing $Disk_{10/2}$ with $Disk_{5/2}$, also 2 mm thick disks, $Disk_{10/2}$ has a greater $f_{l/w}$ than $Disk_{5/2}$. This is because the rate of increase in weight is greater than the rate of increase in lift for $Disk_{5/2}$ than $Disk_{2.5/2}$, while the opposite is true for $Disk_{10/2}$ and $Disk_{5/2}$. The results for 4 mm thick disks are similar.

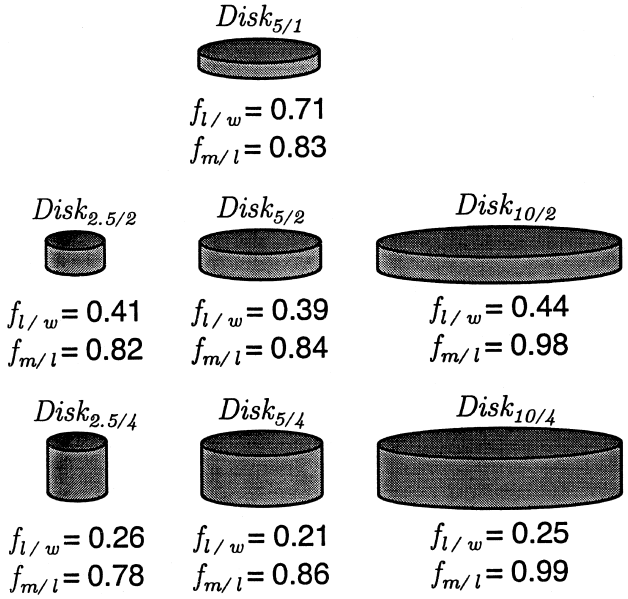

Fig. 14. Values of $f_{l/w}$ and $f_{m/l}$ for seven disks.

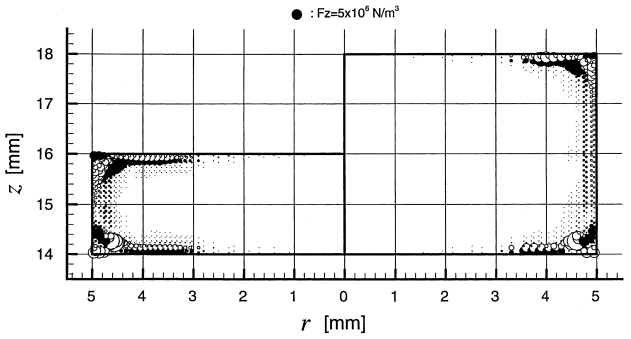

Fig. 15. Lift density distributions for field-cooled ($I_{fc} = 10$ A) $Disk_{5/2}$ (left) and $Disk_{5/4}$ (right) with the magnet energized at 10 A.

In Fig. 14 each disk has $f_{m/l} > 0.75$ and, as stated above, $f_{m/l}$ increases with radius for a given thickness. This implies that most of the lift is due to the external magnetic field and its contribution increases with radius. The difference in the rates in the change of B_z and that of B_r in the z-direction results from different supercurrent distributions in the top and bottom layers and this difference produces lift. The portion of the total lift generated by the field generated by the supercurrent is relatively small, particularly in large disks because in large disks the contribution to the lift by $B_{r_{mag}}$ is large. This difference in contribution to the lift can explain our results presented in the previous paper, [4] where agreement in the results of lift between experiment and computation is better with large disks than with small disks. From these results, we conclude that the magnitude of the B_r component generated by the magnet system is very important and that thinner disks rather than thicker disks can improve lift-to-weight ratio.

Fig. 15 shows lift density distributions for field-cooled ($I_{fc} = 10$ A) $Disk_{5/2}$ (left) and $Disk_{5/4}$ (right) with the magnet energized at 10 A. In each distribution, each right-angled triangular element is assigned a bullet, either black or white, representing force density with its size scaled to the highlighted black bullet of 5×10^6 N/m^3. Each black bullet represents a positive lift density, while each white bullet represents a negative lift density. Note that most of the lift is generated at the corners. This is because the magnitude of $B_{r_{all}}$ – generated by both disk and magnet system – at the top and bottom layers is much larger than that at the middle of the rim, where the field due to the supercurrent in the top layer is canceled by the field due to the supercurrent in the bottom layer.

5. Conclusions

An electromagnetic analysis, based on a three-dimensional FEM applied to the current vector potential method, has been developed to determine the supercurrent distribution in a field-cooled (and hence trapped flux) YBCO disk that levitates stably in a magnetic field generated by the magnet system. The supercurrent distribution thus determined was in turn used to compute trapped-flux-induced field profiles outside the disk and predict a current through the magnet system at which the disk, resting on a support plate, begins to levitate. Agreement between computed field profiles and "levitation" current and those measured in the experiment was excellent, validating the analysis itself and the method used to derive solutions. The analysis demonstrates that the supercurrent distribution within a trapped-flux disk is far more complicated than that derived from the Bean model for a long cylinder under a uniform axial magnetic field. It is used for a parametric study of the effects of disk dimensions (radius, thickness, radius/thickness ratio) and trapped flux strength on supercurrent distribution and lift-to-weight ratio.

Acknowledgements

The authors would like to express their thanks to Dr. M. Murakami and Mr. K. Nagashima of the ISTEC for the YBCO disks used in the experiment; Prof. A. Ishiyama for the use of the Waseda University's computer facilities. YI also thanks the Tokyo Electric Power for the opportunity to spend brief periods of time in 1998 at Keio University; Prof. K. Sawa and his graduate student Mr. K. Nishi of Keio University, for valuable discussion and their preliminary data; Mr. S. Hahakura and Dr. K. Sato of Sumitomo Electric for supplying the HTS electromagnet used in the experiment.

References

[1] Iwasa Y, Lee H. 'Electromaglev' – magnetic levitation of a superconducting disk with a DC field generated by electromagnets. Part 1: theoretical and experimental results on operating modes, lift-to-weight ratio, and suspension stiffness. Cryogenics 1997;37:807.

[2] Iwasa Y, Lee H, Sawa K, Murakami M. Active magnetic levitation with YBCO samples. Advances in superconductivity IX. In: Nakajima S, Murakami M (Eds.), Proceedings of the ninth International Symposium on Superconductivity (ISS'96). 21–24 October 1996, Sapporo. Tokyo: Springer, 1997:1379.

[3] Lee H, Tsuda M, Iwasa Y. 'Electromaglev' ('Active-Maglev') – magnetic levitation of a superconducting disk with a DC field generated by electromagnets. Part 2: theoretical and experimental results on lift-to-weight ratio and lateral stiffness. Cryogenics 1998;38:419.

[4] Tsuda M, Lee H, Iwasa Y. 'Electromaglev' ('Active-Maglev') – magnetic levitation of a superconducting disk with a DC field generated by electromagnets. Part 3: theoretical results on levitation height and stability. Cryogenics 1998;38:743.

[5] Iwasa Y, Lee H, Tsuda M, Murakami M, Miyamoto T, Sawa K, Nishi K, Fujimoto H, Nagashima K. Electromaglev – levitation data for single and multiple bulk YBCO disks. IEEE Trans Appl Superconduc 1999;9:984.

[6] Brandt EH. 'Superconductor disks and cylinders in an axial magnetic field. I. Flux penetration and magnetization curves. Phys Rev B 1998;58(10):6506.

[7] Sanchez A, Navau C. Influence of demagnetizing effects in superconducting cylinders. IEEE Trans Appl Superconduc 1999;9:2195.

[8] Uesaka M, Yoshida Y, Takeda N, Miya K. Experimental and numerical analysis of three-dimensional high-T_c superconducting levitation systems. Int J Appl Electromag Mater 1993;4:13.

[9] Hashizume H, Sugiura T, Miya K, Ando Y, Akita A, Torii S, Kubota Y, Ogasawara T. Numerical analysis of AC losses in superconductors. Cryogenics 1991;31:601.

[10] Noguchi S, Ishiyama A. Optimal design method for MRI superconducting magnets with ferromagnetic shield. IEEE Trans Magn 1997;33(2).